Accepted Manuscript

Low-temperature combustion synthesis of hexagonal $WO_3 \cdot 0.33H_2O$@C as anode material for lithium ion batteries

Zhiwei Liu, Ping Li, Qi Wan, Deyin Zhang, Alex A. Volinsky, Xuanhui Qu

PII: S0925-8388(17)30110-X

DOI: 10.1016/j.jallcom.2017.01.089

Reference: JALCOM 40456

To appear in: *Journal of Alloys and Compounds*

Received Date: 22 June 2016

Accepted Date: 9 January 2017

Please cite this article as: Z. Liu, P. Li, Q. Wan, D. Zhang, A.A. Volinsky, X. Qu, Low-temperature combustion synthesis of hexagonal $WO_3 \cdot 0.33H_2O$@C as anode material for lithium ion batteries, *Journal of Alloys and Compounds* (2017), doi: 10.1016/j.jallcom.2017.01.089.

Low-temperature combustion synthesis of hexagonal $WO_3 \cdot 0.33H_2O$@C as anode material for lithium ion batteries

Zhiwei Liu [a], Ping Li [a]*, Qi Wan [b], Deyin Zhang [a], Alex A. Volinsky [c], Xuanhui Qu [a]

[a] Institute for Advanced Materials and Technology, University of Science and Technology Beijing, Beijing 100083, China.

[b] Energy Material & Technology Research Institute, General Research Institute for Nonferrous Metal, Beijing 100088, China.

[c] Department of Mechanical Engineering, University of South Florida, Tampa, FL 33620, USA.

Abstract

Low temperature combustion route is developed for the synthesis of $WO_3 \cdot 0.33H_2O$ with different amounts of carbon as a composite anode for lithium ion batteries (LIBs). $WO_3 \cdot 0.33H_2O$@C nanoparticles have hexagonal crystal structure. Their electrochemical properties are studied using cyclic voltammetry and galvanostatic charge/discharge cycling. The electrochemical tests demonstrate that the lithium storage capacity of $WO_3 \cdot 0.33H_2O$@C anode has been greatly improved by an appropriate amount of carbon coating, which could maintain a reversible discharge capacity of 816 $mAh \cdot g^{-1}$ after 200 cycles at 100 $mA \cdot g^{-1}$. Its long cycle stability and excellent rate capability are attributed to high electronic conductivity of the appropriate amorphous carbon layer and the unique hexagonal structure of the nanocomposite.

Corresponding author: ustbliping@126.com (P. Li)
Tel: +86-10-82377286; Fax: +86-10-62334311.

Keywords: Low-temperature combustion synthesis; Carbon coated; Anode; Lithium ion batteries.

1. Introduction

Because of the high energy density and good cycling stability, rechargeable lithium ion batteries (LIBs) have attracted considerable attention due to possible applications as power sources for electric vehicles and mobile devices [1-5]. At present, low theoretical capacity of graphite anode (372 $mAh \cdot g^{-1}$) is the main barrier for further LIBs development. Recently many efforts have been devoted to search alternative anode materials to replace graphite in LIBs, so various transition metal oxides have been synthesized and investigated [6-9]. Tungsten oxide-based micro/nanostructured materials have been extensively studied due to their promising applications in photocatalysis [10], gas sensors [11], supercapacitors [12], electrochromic devices [13], dye-sensitized solar cells [14], and lithium ion batteries [15-17]. Nevertheless, the application of tungsten oxides in practical LIBs is seriously hindered due to the relatively large initial irreversible loss and huge volume expansion/contraction during the discharge/charge cycling. In order to solve these limitations, carbon nanocomposites with tungsten oxides have been considered as a reasonable solution.

Tungsten trioxide hydrate ($WO_3 \cdot 0.33H_2O$) is one of the structured materials with promising electrochemical properties [18]. Although substantial research has been conducted in the field of photocatalysis [19-20], there have not been many reports of hexagonal $WO_3 \cdot 0.33H_2O$ nanoparticles used in lithium ion battery applications. Jiao

et al. have reported that symmetrical 3D chrysanthemum-like $WO_3 \cdot 0.33H_2O$ was obtained by the hydrothermal approach, which showed enhanced electrochemical properties [18], but had a problem of charge/discharge capacity of orthorhombic-structured $WO_3 \cdot 0.33H_2O$ attenuating quickly with the number of cycles. One improved strategy to overcome this issue is to prepare nano-sized materials with desired crystal or morphological structure. Therefore, hexagonal $WO_3 \cdot 0.33H_2O$ nanoparticles will show more advantages compared with orthorhombic $WO_3 \cdot 0.33H_2O$ for LIBs.

In this paper, coated hexagonal $WO_3 \cdot 0.33H_2O$ nanoparticles were prepared with different carbon contents via low temperature combustion synthesis. In this design, the hierarchical structure of $WO_3 \cdot 0.33H_2O$@C nanoparticles helps accommodate the volumetric changes during charging/discharging, while the hexagonal crystal structure also facilitates electrolytes and lithium ions transport. The crystal structure, morphology and electrochemical performance have been investigated. The influence of different carbon contents on the charge/discharge properties of the $WO_3 \cdot 0.33H_2O$@C composite is studied.

2. Experimental section

2.1 Materials synthesis

$WO_3 \cdot 0.33H_2O$@C nanoparticles were prepared by low temperature combustion synthesis. In a typical preparation process, ammonium tungstate ($(NH_4)_{10}W_{12}O_{41}$) (0.0075 M, tungsten source), urea ($CO(NH_2)_2$) (0.025 M, fuel), nitric acid (HNO_3) (0.0075 M, oxidant) and appropriate amount of glucose ($C_6H_{12}O_6$) were the organic

agents. A precursor solution was prepared by dissolving all reactants in a sufficient amount of deionized water. The mixture was concentrated in a 500 mL glass and heated in air using an electrical furnace, and evaporated to form a gelatinous mass. When the gelatinous mas swelled, it auto-ignited and initiated a highly exothermic self-contained combustion process, converting gelatinous mass into a loose black mixture. During the combustion process, the glucose molecules underwent dehydration and carbonization reactions, leading to the generation of a carbon layer. The whole process only took several minutes finally resulting in a porous product. According to the molar ratio of glucose and ammonium tungstate, which was 0, 10/3, 15/3 and 20/3, the as-prepared $WO_3 \cdot 0.33H_2O$@C composites were named $WO_3 \cdot 0.33H_2O$, $WO_3 \cdot 0.33H_2O$/C-1, $WO_3 \cdot 0.33H_2O$/C-2, $WO_3 \cdot 0.33H_2O$/C-3, respectively.

2.2 Structure characterization

The phase analysis was performed using X-ray diffraction (XRD, Rigaku D/MAX-RB12) with Cu Kα radiation (λ=1.5406 Å) from 10º to 80º. The morphology of the samples was observed by a field emission scanning electron microscopy (FESEM, Zeiss Ultra 55) and a transmission electron microscopy (TEM, JEOL, JEM-2010). FTIR spectra were recorded using Shimadzu FTIR-8900 spectrophotometer. TG analysis was carried out using Seiko 6300 instrument. The content of the carbon element was measured using an infrared absorption carbon-sulfur analyzer (CS-2008). The BET (QuadraSorb SI) surface area was calculated from nitrogen adsorption isotherm measurements at -196 °C.

2.3 Electrochemical measurements

The electrochemical performance of the samples was measured by assembling coin cells (CR2023) at room temperature. The electrodes are prepared by mixing 60 wt.% active material (the as-synthesized samples), 30 wt.% acetylene black (AB) as a conducting material, and 10 wt.% polyvinylidene fluoride (PVDF) dissolved in N-Methylpyrrolidone (NMP) solution as a binder to form a slurry. The well-mixed slurry was spread onto a Cu foil as a current collector and then dried at 80 °C for 12 h in a vacuum oven. The cells were assembled in Ar filled glove box, using 1 M $LiPF_6$ in ethylene carbonate (EC)/dimethyl carbonate (DMC)/ethyl methyl carbonate (MEC) (1:1:1 by volume) as the electrolyte. The cells were tested by multi-channel land battery test system (LAND CT2001A) in the fixed voltage window from 0.01 V to 3 V at 25 °C. Cyclic voltammetry (CV) were measured using an electrochemical workstation (CHI660C) at a scanning rate of 0.5 $mv \cdot s^{-1}$ in the 0-3 V range at room temperature.

3. Results and discussion

The crystal structure of the as-synthesized $WO_3 \cdot 0.33H_2O$@C composite is characterized by X-ray diffraction, as shown in Fig. 1a. All the detected reflections can be assigned to the hexagonal $WO_3 \cdot 0.33H_2O$ phase with the lattice constants a=b=7.285 Å and c=3.883 Å (JCPDS 35-1001, Fig. 1b). The pattern of $WO_3 \cdot 0.33H_2O$ presents relatively sharp peaks, indicating good crystalline structure of the as-synthesized material without carbon. For the products of $WO_3 \cdot 0.33H_2O$@C composite, the relative intensity of the $WO_3 \cdot 0.33H_2O$ reflections obviously decreased

with carbon content, which is due to the carbon coating on the samples surface. No reflections corresponding to carbon in the $WO_3 \cdot 0.33H_2O$@C composite are observed due to its amorphous nature. It also can be seen that the carbon coating process did not destroy the structure of $WO_3 \cdot 0.33H_2O$.

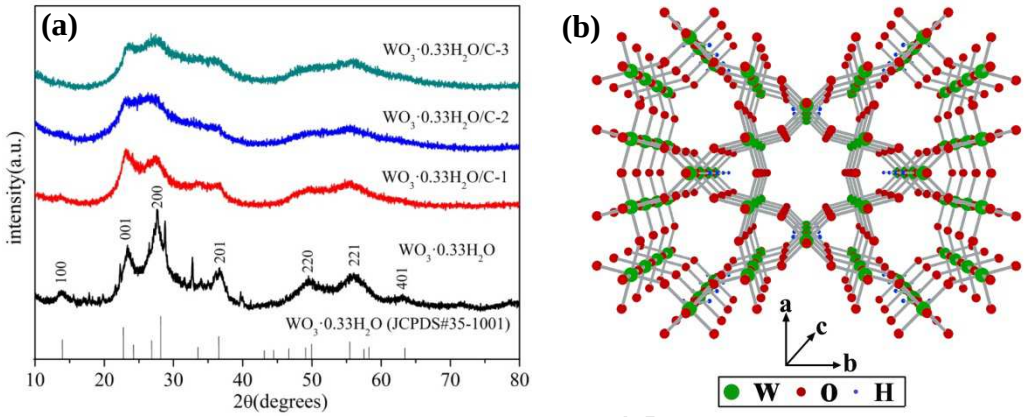

Fig. 1. (a) XRD patterns of $WO_3 \cdot 0.33H_2O$, $WO_3 \cdot 0.33H_2O$/C-1, $WO_3 \cdot 0.33H_2O$/C-2 and $WO_3 \cdot 0.33H_2O$/C-3; (b) hexagonal crystal structure of $WO_3 \cdot 0.33H_2O$.

The structure and morphology of the samples were observed using FESEM and TEM. As seen in Fig. 2a, $WO_3 \cdot 0.33H_2O$ consists of homogeneous and small particles with particle size of about 200 nm. TEM images clearly indicate that $WO_3 \cdot 0.33H_2O$ in Fig. 2b is composed of a lot of small nanoparticles. An average grain size of the nanoparticles is about 10 nm in Fig. 2c, which is consistent with XRD results. The particles size of $WO_3 \cdot 0.33H_2O$/C-1 (Fig. 2d) and $WO_3 \cdot 0.33H_2O$/C-2 (Fig. 2g) decreases with carbon content due to chemical energy release. $WO_3 \cdot 0.33H_2O$/C-1 shows obvious porous agglomerates with many thin grains. From the HRTEM image in Fig. 2f, it should be clear that the grain size and crystallinity of $WO_3 \cdot 0.33H_2O$/C-1 are less than $WO_3 \cdot 0.33H_2O$. As seen in Fig. 2i, a carbon nanolayer of less than 10 nm

thick is on the coated $WO_3 \cdot 0.33H_2O$ surface, which could provide good electronic connection between the nanoparticles. $WO_3 \cdot 0.33H_2O$/C-3 (Fig. 2j-l) shows worse degree of crystallinity with the increasing of carbon content. The amorphous diffraction rings by the selected area electron diffraction (SAED) pattern in Fig. 2l may be ascribed to the lower degree of $WO_3 \cdot 0.33H_2O$/C-3 crystallinity and a lot of amorphous carbon.

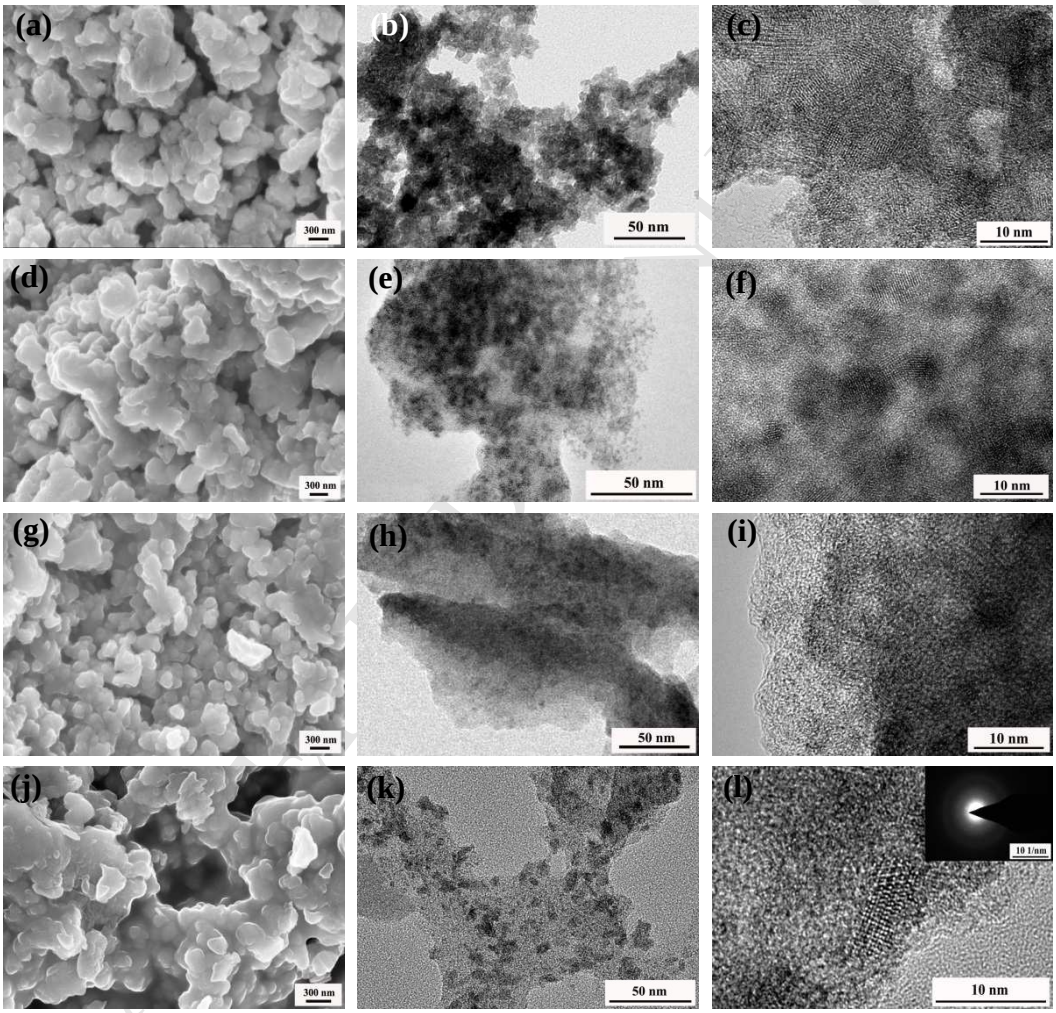

Fig. 2. FESEM and TEM images of (a-c) $WO_3 \cdot 0.33H_2O$, (d-f) $WO_3 \cdot 0.33H_2O$/C-1, (g-i) $WO_3 \cdot 0.33H_2O$/C-2 and (j-l) $WO_3 \cdot 0.33H_2O$/C-3.

The FT-IR spectra of the prepared samples are shown in Fig. 3. The $WO_3 \cdot 0.33H_2O$ spectra show strong and wide absorption peak at 3133 cm^{-1}, which

corresponds to -OH stretching vibration, resulting from the hydrogen bond association of crystal water and the presence of adsorption water on the surface of the $WO_3 \cdot 0.33H_2O$ nanoparticles. The absorption peak at 1628 cm^{-1} is assigned to H-O-H bending vibration. Another absorption peak at 1383 cm^{-1} corresponds to N-O bending vibration due to the incomplete reaction of nitrate ion. The characteristic peak at 829 cm^{-1} is responsible for corner-shared W-O-W extending vibration, revealing the presence of the W-O bond in the $WO_3 \cdot 0.33H_2O$ crystal structure [21]. These strong absorption peaks are attributed to the high degree of $WO_3 \cdot 0.33H_2O$ crystallinity. In the FT-IR spectrum of $WO_3 \cdot 0.33H_2O$/C-1, the band in the 3424 cm^{-1} region is assigned to the O-H stretching vibrations of coordinated water and the band at 2361 cm^{-1} is assigned to the N-H stretching vibrations of the residual $(NH_2)^{2-}$. The reduced peaks intensity at 1628 cm^{-1} and 1384 cm^{-1} are due to complete reaction of raw materials. Similar spectra are recorded for $WO_3 \cdot 0.33H_2O$/C-3 with a characteristic IR bands at 3424 cm^{-1}, 2361 cm^{-1}, 1628 cm^{-1} and 1384 cm^{-1}. In the case of $WO_3 \cdot 0.33H_2O$/C-2, the absorption peaks at 809 cm^{-1} and 627 cm^{-1} are attributed to C-H bending vibrations, due to the presence of residual glucose.

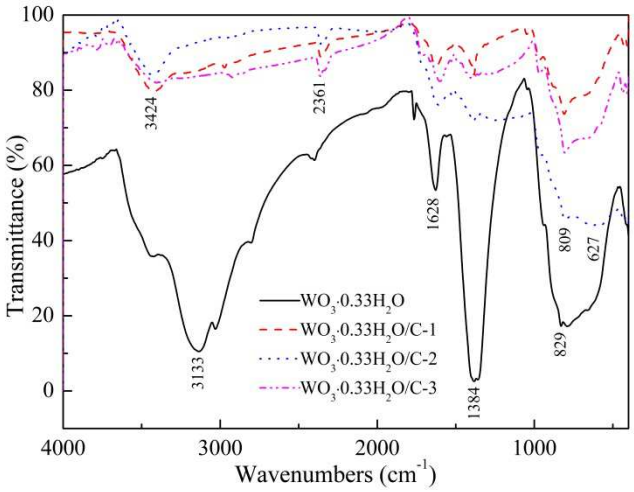

Fig. 3. FT-IR spectra of $WO_3 \cdot 0.33H_2O$, $WO_3 \cdot 0.33H_2O$/C-1, $WO_3 \cdot 0.33H_2O$/C-2 and $WO_3 \cdot 0.33H_2O$/C-3.

Thermal decomposition of the samples is monitored using TG methods in Fig. 4. Slight $WO_3 \cdot 0.33H_2O$ weight loss between 50 °C and 190 °C can be attributed to adsorbed water on the sample surface [22]. An obvious weight loss is detected between 190 °C and 270 °C, which can be due to the loss of hydration water. Slight weight loss between 270 °C and 410 °C results from the complete removal of hydration water, which suggests that $WO_3 \cdot 0.33H_2O$ completely transformed into WO_3. When the temperature is higher than 410 °C, the weight of the sample is practically unchanged. The as-prepared $WO_3 \cdot 0.33H_2O$/C-1 shows a rapid weight loss from 50 °C to 150 °C, which is due to the existence of the adsorbed water. A slight weight loss between 150 °C and 410 °C is due to the removal of hydration water. For the 410-700 °C temperature range, continuous weigh loss corresponds to the removal of carbon from the sample as CO_2 [23]. Fast weigh loss over 700 °C indicates that the carbonization process of tungsten trioxide occurred. The TG curves of $WO_3 \cdot 0.33H_2O$/C-2 and $WO_3 \cdot 0.33H_2O$/C-3 are similar to the curve of

$WO_3 \cdot 0.33H_2O$/C-1. Then $WO_3 \cdot 0.33H_2O$/C-3 shows a higher weight loss rate.

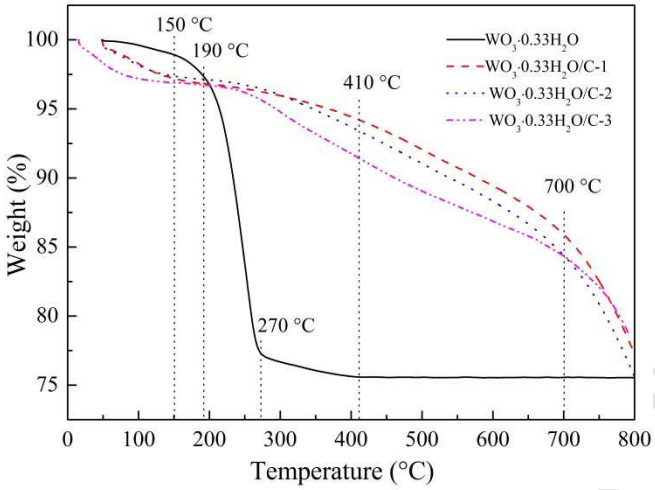

Fig. 4. TG data of $WO_3 \cdot 0.33H_2O$, $WO_3 \cdot 0.33H_2O$/C-1, $WO_3 \cdot 0.33H_2O$/C-2 and $WO_3 \cdot 0.33H_2O$/C-3.

The specific surface areas of $WO_3 \cdot 0.33H_2O$ and $WO_3 \cdot 0.33H_2O$/C-2 are investigated using nitrogen adsorption/desorption isotherms (Fig. 5a). Both samples show representative type IV isotherms with an obvious hysteresis loop, indicating the presence of mesoporous structures. The specific surface area of $WO_3 \cdot 0.33H_2O$ is 3.456 $g \cdot m^{-2}$, which is higher than $WO_3 \cdot 0.33H_2O$/C-2 (Table 1). Moreover, as seen in Fig. 5b, the pore size distribution estimated by the BJH analysis shows that the maximum diameters of $WO_3 \cdot 0.33H_2O$ and $WO_3 \cdot 0.33H_2O$/C-2 are 3.805 nm and 3.419 nm, respectively. Compared with $WO_3 \cdot 0.33H_2O$, the BET surface area of $WO_3 \cdot 0.33H_2O$/C-2 is obviously decreased due to the carbon coating on $WO_3 \cdot 0.33H_2O$ particles forming carbon walls. The presence of mesopores in the samples improves electrolyte and ion diffusion in the process of Li^+ insertion/extraction. Due to the influence of amorphous carbon, the low specific surface area of the samples could hinder the reaction between active materials and

electrolyte at the early stages. The C content of the samples is shown in Table 1. The C content of $WO_3 \cdot 0.33H_2O$/C-1, $WO_3 \cdot 0.33H_2O$/C-2 and $WO_3 \cdot 0.33H_2O$/C-3 is about 11.2 wt.%, 15.9 wt.% and 23.8 wt.%, respectively, which is consistent with the added content of glucose.

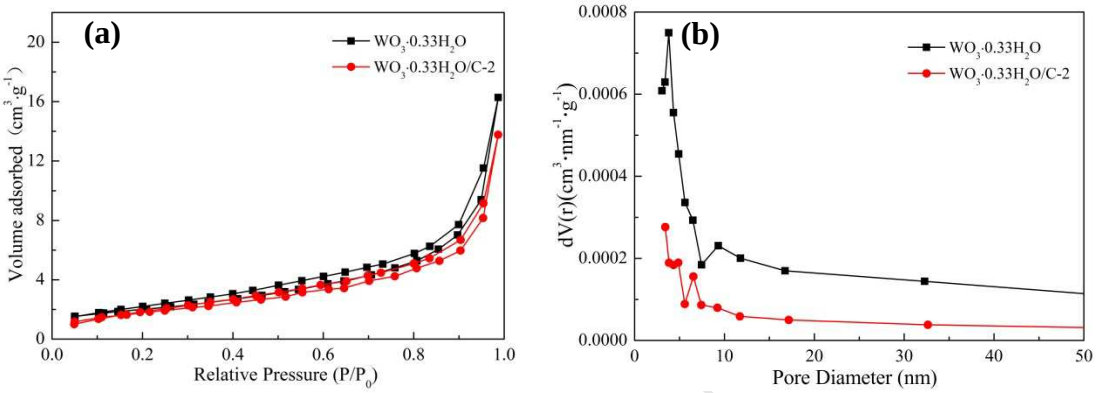

Fig. 5. (a) Nitrogen adsorption/desorption isotherms and (b) pore size distribution of $WO_3 \cdot 0.33H_2O$ and $WO_3 \cdot 0.33H_2O$/C-2.

Table. 1. C contents and BET of the prepared samples.

Sample	C contents (wt.%)	BET ($g \cdot m^{-2}$)
$WO_3 \cdot 0.33H_2O$	0	3.456
$WO_3 \cdot 0.33H_2O$/C-1	11.2	1.713
$WO_3 \cdot 0.33H_2O$/C-2	15.9	1.284
$WO_3 \cdot 0.33H_2O$/C-3	23.8	0.982

Fig. 6 shows CV curves of the sample electrodes in a potential window of 0.01-3 V at a scanning rate of 0.5 $mV \cdot s^{-1}$ for the first 3 cycles. In the first cycle of the $WO_3 \cdot 0.33H_2O$ electrode, cathodic peaks are observed at 1.3 V, 0.25 V and 0.01 V, respectively, corresponding to electrochemical reduction reaction of $WO_3 \cdot 0.33H_2O$

with Li^+ ($WO_3 \cdot 0.33H_2O + xLi \rightarrow Li_xWO_3 \cdot 0.33H_2O$, $Li_xWO_3 \cdot 0.33H_2O + (6\text{-}x)\ Li \rightarrow W + 3Li_2O + 0.33H_2O$). However, only one cathodic peak is noticed at 0.25 V and 0.6 V during the second and third cycles. In contrast, the anodic peaks at 1.1 V, 1.6 V and 2.8 V during the charging process are ascribed to the decomposition reaction of Li_2O [17]. Apparently, the electrochemical reaction of $WO_3 \cdot 0.33H_2O$ with Li^+ involved multi-steps for its decomposition and formation. For the first cycle of the $WO_3 \cdot 0.33H_2O$/C-1 electrode, cathodic peaks at 0.6 V, 0.01 V and anodic peaks at 1.1 V are observed. The cathodic peak at 0.6 V disappeared in the subsequent cycles, which could be due to an irreversible process. Meanwhile, the cathodic peak at 0.8 V and the anodic peak at 1.1 V consisted of the reversible conversion reaction in Li^+ insertion/extraction process. The CV curves of $WO_3 \cdot 0.33H_2O$/C-2 and $WO_3 \cdot 0.33H_2O$/C-3 electrodes are basically consistent with the $WO_3 \cdot 0.33H_2O$/C-1 electrode. Compared with the $WO_3 \cdot 0.33H_2O$ electrode, characteristic peaks of carbon coated $WO_3 \cdot 0.33H_2O$ electrode are obviously different, which is due to the presence of carbon layer. The existence of coated carbon has effectively reduced the oxidation potential of $WO_3 \cdot 0.33H_2O$@C electrode, which stabilizes the electrode reaction and increases electronic conductivity.

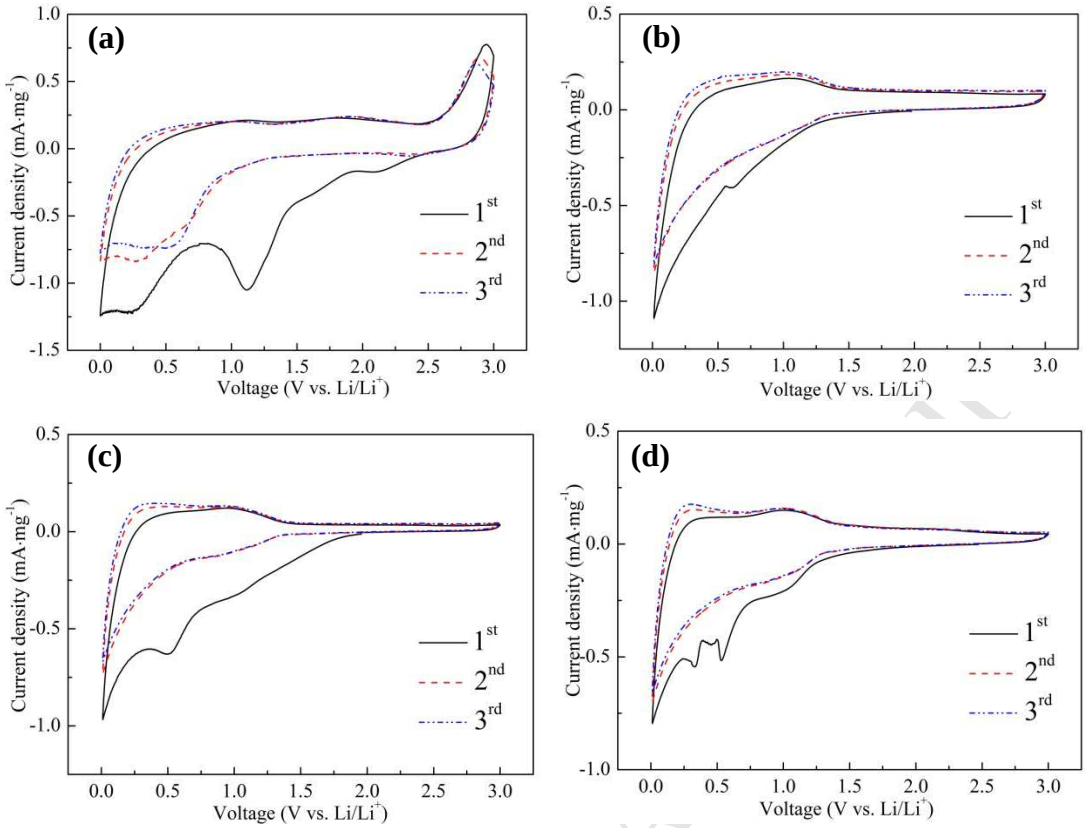

Fig. 6. Cycle voltammetry curves of: (a) $WO_3 \cdot 0.33H_2O$; (b) $WO_3 \cdot 0.33H_2O$/C-1; (c) $WO_3 \cdot 0.33H_2O$/C-2; (d) $WO_3 \cdot 0.33H_2O$/C-3 in the voltage range of 0.01-3 V at a scan rate of 0.5 mV·s^{-1}.

Fig. 7 shows the charge/discharge curves of $WO_3 \cdot 0.33H_2O$, $WO_3 \cdot 0.33H_2O$/C-1, $WO_3 \cdot 0.33H_2O$/C-2 and $WO_3 \cdot 0.33H_2O$/C-3 at a current density of 100 mA·g^{-1} between 0.01 V and 3 V (vs. Li/Li^+). The open circuit voltage of the cells is about 2.8 V. Three discharge voltage plateaus (1.4 V, 0.6 V and 0.01 V) and two charge voltage plateaus (1.1 V and 2.8V) are observed for the $WO_3 \cdot 0.33H_2O$ electrode, which are due to the electrochemical behavior of the electrode with lithium. The initial discharge and charge capacity is 1543 and 711 mAh·g^{-1}, respectively, much higher than the calculated value for tungsten oxide materials (693 mAh·g^{-1}). The irreversible capacity loss of the first cycle could partly result from the formation of the SEI layer at the

electrode-electrolyte interface [24], further lithium storage via interfacial charging at the metal/Li_2O interface [25]. The formation of lithium oxides results in the continuous growth of lithium consumption during the discharge process [26]. The subsequent discharge and charge curves are smooth and stable. For the initial cycle of $WO_3 \cdot 0.33H_2O$/C-1, $WO_3 \cdot 0.33H_2O$/C-2 and $WO_3 \cdot 0.33H_2O$/C-3 electrodes, there are two discharge voltage plateaus (0.8 and 0.01 V) and one charge voltage plateau (1.1 V) observed during the initial charge/discharge process. The obvious difference in the initial charge/discharge capacity indicates that the amount of carbon would necessarily lead to a decrease in theoretical capacity because it does not contribute to or lower the theoretical lithium storage capacity [27]. However, $WO_3 \cdot 0.33H_2O$/C-2 electrode shows the best cycle performance, exhibiting the highest discharge/charge capacity of 816/808 $mAh \cdot g^{-1}$ at the 200^{th} cycles. This result further confirms that $WO_3 \cdot 0.33H_2O$/C-2 is structurally stable during the repeated electrochemical reactions.

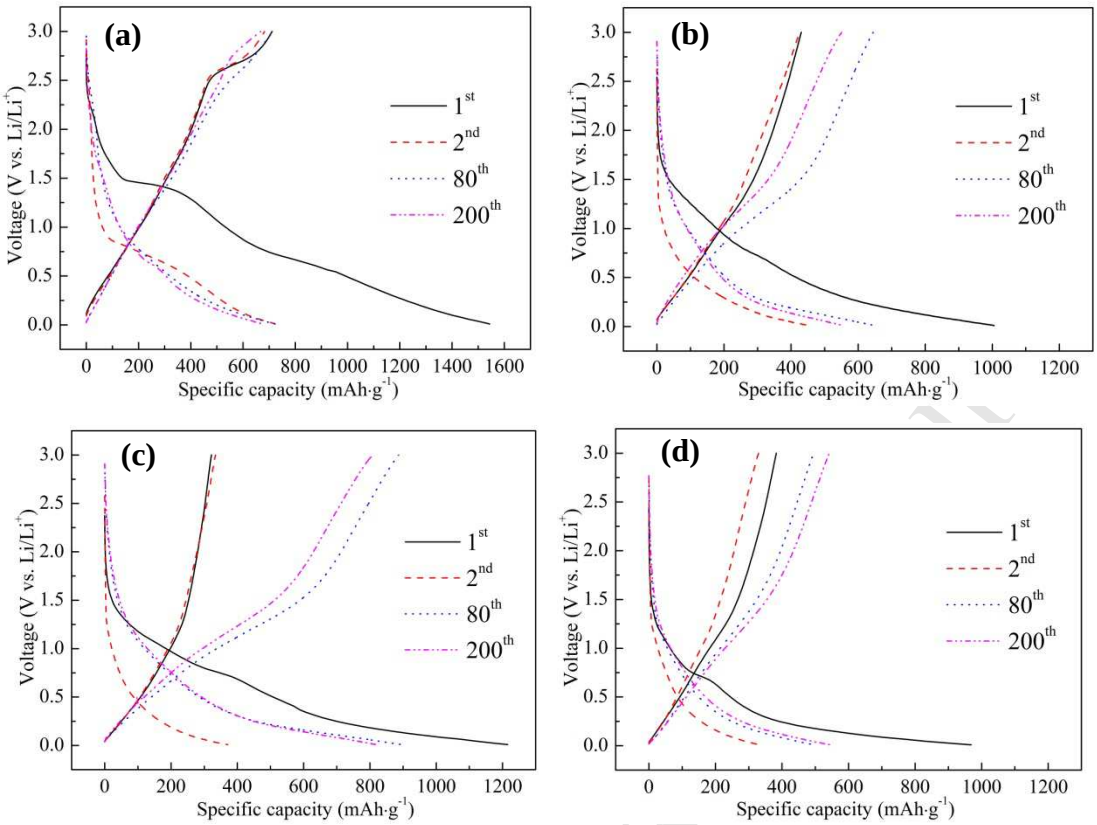

Fig. 7. Charge/discharge curves of: (a) $WO_3 \cdot 0.33H_2O$; (b) $WO_3 \cdot 0.33H_2O$/C-1; (c) $WO_3 \cdot 0.33H_2O$/C-2; (d) $WO_3 \cdot 0.33H_2O$/C-3 in the 0.01-3 V voltage range at 100 $mA \cdot g^{-1}$ current density.

The cyclability of $WO_3 \cdot 0.33H_2O$, $WO_3 \cdot 0.33H_2O$/C-1, $WO_3 \cdot 0.33H_2O$/C-2 and $WO_3 \cdot 0.33H_2O$/C-3 at a current density of 100 $mA \cdot g^{-1}$ is shown in Fig. 8a. $WO_3 \cdot 0.33H_2O$ electrodes shows a relatively stable discharge/charge capacity of 642/636 $mAh \cdot g^{-1}$ after 200 cycles, which is dramatically higher than the orthorhombic $WO_3 \cdot 0.33H_2O$ reported to date [18]. Good cyclability could be due to its special hexagonal structure. Huge hexagonal cavity provides efficient electrical and ionic transfer pathways, which contribute to the improved reversible capacity and capability [22]. The $WO_3 \cdot 0.33H_2O$/C-1 electrode presents a lower discharge/charge capacity of 557/551 $mAh \cdot g^{-1}$ after 200^{th} cycle, which might due to a small amount of carbon

sacrificing some lithium storage. Compared with $WO_3 \cdot 0.33H_2O$, the $WO_3 \cdot 0.33H_2O$/C-2 electrode shows capacity increase until the 80^{th} cycle, corresponding to the activation process during the charge/discharge reaction [28]. The outer carbon layer can be regarded as a buffer, which can prevent contiguous active materials from contacting each other and the electrolyte. After 200 cycles, the discharge capacity of $WO_3 \cdot 0.33H_2O$/C-2 still remains at 816 $mAh \cdot g^{-1}$, indicating excellent cycling performance of the $WO_3 \cdot 0.33H_2O$/C-2 electrode. The enhanced electrochemical performance of the $WO_3 \cdot 0.33H_2O$/C-2 in comparison with $WO_3 \cdot 0.33H_2O$ could be attributed to the appropriate amount of carbon. The carbon layer minimizes the massive volume expansion, improves the electrical conductivity and facilitates the formation of stable SEI [29]. The rate capability of $WO_3 \cdot 0.33H_2O$ and $WO_3 \cdot 0.33H_2O$/C-2 electrodes is studied at different rates ranging from 100 $mA \cdot g^{-1}$ to 5000 $mA \cdot g^{-1}$ after 100 cycles, as seen in Fig. 8b. The $WO_3 \cdot 0.33H_2O$/C-2 electrode shows superior rate performance, with discharge capacity of 906 $mAh \cdot g^{-1}$, 767 $mAh \cdot g^{-1}$, 594 $mAh \cdot g^{-1}$, 275 $mAh \cdot g^{-1}$, 151 $mAh \cdot g^{-1}$ and 114 $mAh \cdot g^{-1}$ at 100 $mA \cdot g^{-1}$, 200 $mA \cdot g^{-1}$, 500 $mA \cdot g^{-1}$, 1000 $mA \cdot g^{-1}$, 2000 $mA \cdot g^{-1}$ and 5000 $mA \cdot g^{-1}$, respectively. The improved rate performance is most likely due to the excellent electronic conductivity of the carbon layer.

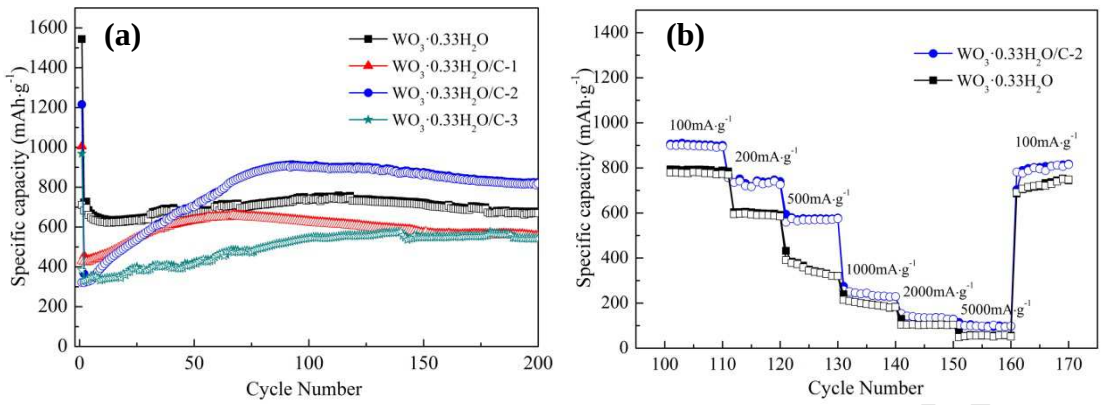

Fig. 8. (a) Cycling performance of $WO_3 \cdot 0.33H_2O$, $WO_3 \cdot 0.33H_2O$/C-1, $WO_3 \cdot 0.33H_2O$/C-2 and $WO_3 \cdot 0.33H_2O$/C-3 at 100 mA·g^{-1}; (b) Rate performance of $WO_3 \cdot 0.33H_2O$ and $WO_3 \cdot 0.33H_2O$/C-2 after 100 cycles.

4. Conclusions

In summary, we report nano-sized $WO_3 \cdot 0.33H_2O$@C anode material for high performance lithium ion batteries, which is prepared by the solution combustion synthesis. $WO_3 \cdot 0.33H_2O$@C nanoparticles exhibit hexagonal crystal structure, which can provide efficient channels and more active sites for the fast transport of electrons and ions. The $WO_3 \cdot 0.33H_2O$/C-2 electrode shows high reversible discharge capacity of 816 mAh·g^{-1} after 200 cycles at 100 mA·g^{-1}. Its long cycle stability and excellent rate capability are attributed to high electronic conductivity of the appropriate amorphous carbon layer and unique hexagonal structure of the nanocomposite. High electrochemical performance makes it a promising anode material for LIBs.

References

[1] A. S. Arico, P. Bruce, B. Scrosati, J. M. Tarascon, W. V. Schalkwijk, Nat. Mater. 4 (2005) 366-377.

[2] G. L. Cui, L. J. Zhi, A. Thomas, U. Kolb, I. Lieberwirth, K. Müllen, Angew. Chem.

Int. Ed. 46 (2007) 3464-3467.

[3] J. Wang, Y. S. He, J. Yang, Adv. Mater. 27 (2015) 569-575.

[4] Y. Yao, M. T. McDowell, I. Ryu, H. Wu, N. Liu, L. B. Hu, William. D. Nix, Y. Cui, Nano Lett. 11 (2011) 2949-2954.

[5] J. Jiang, Y. Y. Li, J. P. Liu, X. T. Huang, C. Z. Yuan, X. W. Lou, Adv. Mater. 24 (2012) 5166-5180.

[6] Q. S. Xie, Y. T. Ma, D. Q. Zeng, X. Q. Zhang, L. S. Wang, G. H. Yue, D. L. Peng, ACS Appl. Mater. Interfaces 6 (2014) 19895-19904.

[7] X. L. Xiao, X. F. Liu, H. Zhao, D. F. Chen, F. Z. Liu, J. H. Xiang, Z. B. Hu, Y. D. Li, Adv. Mater. 24 (2012) 5762-5766.

[8] J. X. Zhu, Z. Y. Yin, D. Yang, T. Sun, H. Yu, H. E. Hoster, H. H. Hng, H. Zhang, Q. Y. Yan, Energy Environ. Sci. 6 (2013) 987-993.

[9] H. Huang, T. Feng, Y. P. Gan, M. Y. Fang, Y. Xia, C. Liang, X. Y. Tao, W. K. Zhang, ACS Appl. Mater. Interfaces 7 (2015) 11842-11848.

[10] X. H. Zhang, X. H. Lu, Y. Q. Shen, J. B. Han, L. Y. Yuan, L. Gong, Z. Xu, X. D. Bai, M. Wei, Y. X. Tong, Y. H. Gao, J. Chen, J. Zhou, Z. L. Wang, Chem. Commun. 47 (2011) 5804-5806.

[11] J. M. Ma, J. Zhang, S. R. Wang, T. H. Wang, J. B. Lian, X. C. Duan, W. J. Zheng, J. Phys. Chem. C 115 (2011) 18157-18163.

[12] S. H. Yoon, E. Kang, J. K. Kim, C. W. Lee, J. Lee, Chem. Commun. 47 (2011) 1021-1023.

[13] W. Wang, Y. X. Pang, S. N. B. Hodgson, J. Mater. Chem. 20 (2010) 8591-8599.

[14] H. D. Zheng, Y. Tachibana, K. Kalantar-Zadeh, Langmuir 26 (2010) 19148-19152.

[15] W. J. Li, Z. W. Fu, Appl. Surf. Sci. 256 (2010) 2447-2452.

[16] Z. J. Gu, H. Q. Li, T. Y. Zhai, W. S. Yang, Y. Y. Xia, Y. Ma, J. N. Yao, J. Solid State Chem. 180 (2007) 98-105.

[17] S. H. Yoon, C. S. Jo, S. Y. Noh, C. W. Lee, J. H. Song, J. Lee, Phys. Chem. Chem. Phys. 13 (2011) 11060-11066.

[18] J. Q. Yang, L. F. Jiao, Q. Q. Zhao, Q. H. Wang, H. Y. Gao, Q. N. Huan, W. J. Zheng, Y. J. Wang, H. T. Yuan, J. Mater. Chem. 22 (2012) 3699-3701.

[19] J. Y. Li, J. F. Huang, J. P. Wu, L. Y. Cao, Q. J. Li, K. Yanagisawa, Cryst. Eng. Comm. 15 (2013) 7904-7913.

[20] X. Y. He, C. G. Hu, Q. N. Yi, H. Hua, X. Y. Li, Catal. Lett. 142 (2012) 637-645.

[21] G. Ramis, C. Cristiani, A. S. Elmi, P. Villa, J. Mol. Catal. 61 (1990) 319-331.

[22] L. Liu, H. P. Guo, M. Zhou, Q. L. Wei, Z. H. Yang, H. B. Shu, X. K. Yang, J. L. Tan, Z. C. Yan, X. Y. Wang, J. Power Sources 238 (2013) 501-515.

[23] S. Yoon, S. G. Woo, K. N. Jung, H. Song, J. Alloys Compd. 613 (2014) 187-192.

[24] P. Balaya, H. Li, L. Kienle, J. Maier, Adv. Funct. Mater. 13 (2003) 621-625.

[25] Y. C. Qiu, G. L. Xu, K. Y. Yan, H. Sun, J. W. Xiao, S. H. Yang, S. G. Sun, L. M. Jin, H. Deng, J. Mater. Chem. 21 (2011) 6346-6353.

[26] G. L. Xu, Y. Li, T. Y. Ma, Y. Ren, H. H. Wang, L. F. Wang, J. G. Wen, D. Miller, K. Amine, Z. H. Chen, Nano Energy 18 (2015) 253-264.

[27] G. Chen, M. Zhou, J. Catanach, T. Liaw, L. Fei, S. G. Deng, H. M. Luo, Nano

Energy 8 (2014) 126-132.

[28] M. H. Ryu, K. N. Jung, K. H. Shin, K. S. Han, S. Yoon, J. Phys. Chem. C 117 (2013) 8092-8098.

[29] H. Wu, N. Du, J. Z. Wang, H. Zhang, D. R. Yang, J. Power Sources 246 (2014) 198-203.

Highlights

1. $WO_3 \cdot 0.33H_2O$@C was prepared by low-temperature combustion synthesis.

2. Specific structure can provide efficient channels for fast Li^+ transport.

3. Appropriate amorphous carbon layer can improve lithium storage capacity.